UNIVERSITÄT AUGSBURG
Universitätsbibliothek

OPEN ACCESS
OPUS AUGSBURG

Synthesis and characterization of nanocrystalline SrTiO3

Palani Balaya, Martin Ahrens, Lorentz Kienle, Joachim Maier, Behnaz Rahmati, Sung Bo Lee, Wilfried Sigle, Alexej Pashkin, Christine A. Kuntscher, Martin Dressel

Angaben zur Veröffentlichung / Publication details:

Balaya, Palani, Martin Ahrens, Lorentz Kienle, Joachim Maier, Behnaz Rahmati, Sung Bo Lee, Wilfried Sigle, Alexej Pashkin, Christine A. Kuntscher, and Martin Dressel. 2006. "Synthesis and characterization of nanocrystalline SrTiO3." *Journal of the American Ceramic Society* 89 (9): 2804–11. https://doi.org/10.1111/j.1551-2916.2006.01133.x.

Nutzungsbedingungen / Terms of use:

licgercopyright

Dieses Dokument wird unter folgenden Bedingungen zur Verfügung gestellt: / This document is made available under these conditions:
Deutsches Urheberrecht
Weitere Informationen finden Sie unter: / For more information see:
https://www.uni-augsburg.de/de/organisation/bibliothek/publizieren-zitieren-archivieren/publiz/

Synthesis and Characterization of Nanocrystalline $SrTiO_3$

Palani Balaya,† Martin Ahrens, Lorentz Kienle, and Joachim Maier*

Max Planck Institute for Solid State Research, D-70569 Stuttgart, Germany

Behnaz Rahmati, Sung Bo Lee, and Wilfried Sigle

Max Planck Institute for Metal Research, D-70569 Stuttgart, Germany

Alexej Pashkin, Christine Kuntscher, and Martin Dressel

Institute of Physics, University of Stuttgart, D-70550 Stuttgart, Germany

The synthesis and densification of fairly dense nanocrystalline $SrTiO_3$ and its characterization are described in this paper in detail. Significant grain growth was avoided by the application of a two-stage sintering process using hot pressing. High-resolution transmission electron microscopy and electron energy loss spectroscopy characterizations indicate pure material with no detectable chemical inhomogeneities. The electrical measurements indicate the disappearance of bulk contribution to the electrical conduction due to the overlap of depleted space charge layers if the grain size is below 100 nm. Owing to the overlap, the capacitance appears as bulk-like rather than due to space charge polarization. Non-contact sub-millimeter optical spectroscopy measurements reveal strong suppression of the dielectric constant values at low temperature.

I. Introduction

NANOCRYSTALLINE materials have triggered great excitement concerning technological relevance but also fundamental impact. While electronic materials are widely investigated at nano-size,[1–3] this is not so much the case for ionically as well as mixed conducting materials, although they play a significant role in a variety of applications such as batteries, fuel cells, and sensors. Even though classical in nature, nano-ionic effects are by no means less striking[4–8]; here, we only mention the ionic conduction behavior in nanometer-sized CaF_2/BaF_2 multilayers,[9] the change of the conduction mechanism from ionic to electronic in dense nanocrystalline ceria,[10] or the anomalous storage of Li in nanocomposites.[11]

$SrTiO_3$ has attracted much attention due to both scientific and technological considerations. $SrTiO_3$ is a useful material for sensors, photo-electrodes, varistors, and many other applications. From a fundamental point of view, $SrTiO_3$ is a model oxide for mixed ionic and electronic conduction. In both cases, the space charge layers at grain-boundary cores are of significant interest. The electrical properties of high- and low-angle grain-boundary cores of Fe-doped $SrTiO_3$ bicrystals are investigated in great detail.[12–20] These grain-boundary cores have been found to be positively charged and hence to be accompanied by zones in which electron holes ($h^\bullet$) and oxygen vacancies ($V_O^{\bullet\bullet}$) are depleted, the concentration of the latter ($[V_O^{\bullet\bullet}]$) being depleted more strongly, because of the double charge leading to a quadratic effect compared with the hole depletion.[20] The defect concentrations in the grain-boundary zones are thus grossly different from the bulk. While the electrical properties of both bulk and grain boundary are well studied in bicrystals and microcrystals, it remained a challenge to study the electrical conduction in nanocrystalline $SrTiO_3$ (with grain sizes less than 100 nm) in which the grain size turns out to be comparable with the space charge width. This situation is referred to as "mesoscopic situation"[21] (the reasons for the large screening lengths are the low charge carrier density and the high dielectric constant). So far, sufficiently dense nanocrystalline $SrTiO_3$ ceramics have not been available. In this paper, we describe their synthesis and characterization and briefly touch upon the electrical behavior. A more detailed discussion of the electrical conductivity has been given elsewhere.[21]

For the investigation of electrical properties of electroceramics such as $SrTiO_3$, $BaTiO_3$, ZnO, etc., it is mandatory to fabricate samples with high density. Two important criteria required to be fulfilled for achieving dense nanocrystalline $SrTiO_3$ are (a) to synthesize very fine particles as the final average grain size of the sintered specimen depends on the particle size of the nanopowder itself, and, most challenging in many cases, (b) to achieve dense compaction during sintering that avoids excessive grain growth and retains nanocrystallinity.

Various wet-chemical methods have been reported in the literature[22–28] for the synthesis of $SrTiO_3$ nanopowders: the polymerized complex (PC) method, the microemulsion method, the hydrothermal synthesis, the stearic acid sol–gel method, the solution–precipitation method, and the combustion synthesis using ethylene diamine tetraacetic acid (EDTA) and NH_3(aq.). Our experience is that the $SrTiO_3$ synthesized through sol–gel techniques suffers from the presence of unavoidable traces of carbon. In addition, strongly agglomerated nanoparticles with a significant fraction of porosity have been observed due to the exothermic reaction during the burning process of the organics. Such fine powders with high porosity could not be compacted to a high-density pellet. There is hardly any report available in the literature about the synthesis of pure $SrTiO_3$ nanopowder followed by successful densification. If, e.g., the powder synthesized by the stearic acid sol–gel technique[25] is calcined at 1000°C for 1 h, the particle size increases up to 120 nm. In this paper, we report an optimized synthesis technique for achieving nominally pure $SrTiO_3$ nanopowder ($\sim$30 nm) and to arrive at dense nanoceramics of $SrTiO_3$ with an average grain size of 80 nm. In addition, we also characterize the nanoceramic $SrTiO_3$ using high-resolution transmission electron microscopy (HRTEM) and electron energy loss spectroscopy (EELS), focusing on the grain-boundary structure and composition. A most striking result of the electrical characterization is that for 80 nm grain size the bulk response to the electrical conduction disappears due to overlap of depleted space charge regions.

*Member, American Ceramic Society.
†Author to whom correspondence should be addressed. e-mail: p.balaya@fkf.mpg.de

II. Experimental Procedure

(1) Synthesis

For the synthesis of $PbTiO_3$, Camargo and Kakihana[29] used the peroxy-based route (PBR) that has the advantage of eliminating traces of chlorine impurities. Applying this synthesis procedure for $SrTiO_3$ nanoparticles yielded powders with a grain size of nearly 50 nm. Although X-ray diffraction (XRD) confirmed the formation of $SrTiO_3$ phase, analysis of the Sr and Ti contents from an inductively coupled plasma (ICP) spectroscopy experiment revealed excess Ti content as compared with Sr. One possible reason for this non-stoichiometry is probably that Ti and Sr do not take part in the reaction completely. We further modified the PBR by introducing an EDTA complexing agent as indicated in the flow chart (Fig. 1) so that Ti and Sr precursors form Ti–EDTA and Sr–EDTA complexes. It may be noted that we have made no further attempt to identify these complexes, as this is beyond the scope of this paper. However, it is realized that this modified peroxy-based method (described below in detail) indeed enables one to obtain a homogeneous mixture of an equal amount of Sr and Ti, thus leading to the formation of a stoichiometric $SrTiO_3$ compound.

Figure 1 presents the flow chart of the modified peroxy-based method developed for the synthesis of the $SrTiO_3$ nanopowder. This procedure avoids a major problem of the formation of amorphous TiO_2 experienced while using titanium tetrabutoxide or titanium tetraisopropoxide or titanium tetrachloride as a precursor in an aqueous environment. A Ti metal foil and $Sr(NO_3)_2$ were used as precursor materials for synthesis in the aqueous medium. The Ti metal foil (purity: 99.7%; thickness: 30 μm; Alfa Aesar, Karlsruhe, Germany) was dissolved in a mixture of hydrogen peroxide (30%) and ammonia solution (65%) whose pH was adjusted to be 11 and the reaction temperature was maintained below 10°C using an ice bath to avoid evaporation of ammonia. The metal foils dissolved completely after 5 h of continuous stirring and resulted in a yellow-colored solution of peroxytitanato acid $[Ti(OH)_3O_2]^-$. One mole of EDTA per Ti was added to the above solution and stirred for 10 min for a complete dissolution. Following this, 40 mL of distilled water was added and the stirring continued for another 10 min. In addition, one more mole of EDTA was added and vigorous stirring was continued for further 10 min. The pH of the whole solution was adjusted at this stage to 7 by adding HNO_3. A yellowish solution was obtained after continuous stirring for about 30 min. One mole of $Sr(NO_3)_2$ (99.995%, Alfa Aesar), dissolved in 20 mL of distilled H_2O, was added to this solution. The reaction set in instantly and resulted in the formation of a light green-colored precipitate of a Sr–Ti complex. The stirring continued for about 15 h at a temperature of ice water, from which a clear pale-green-colored precipitate was obtained.

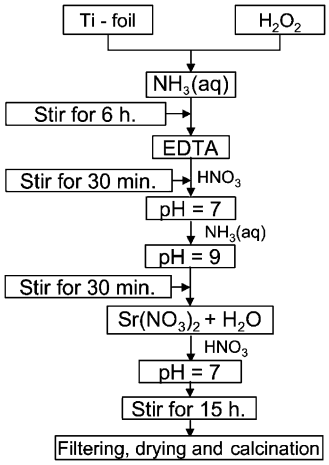

Fig. 1. Flow chart for synthesizing $SrTiO_3$ nanopowder using a modified peroxy-based route.

The precipitate thus obtained was filtered, dispersed in distilled H_2O, and then centrifuged. The latter procedure was repeated four times, in order to remove traces of NO_3 and NH_4. The product was found to be a light-green-colored thick gel. This wet precipitate was further dried under vacuum (1 mbar) at 80°C for about 12 h. Upon gentle grinding of this dried product, a fluffy light-greenish precipitate powder was obtained, which was subsequently subjected to the thermal analysis to determine the decomposition temperature of the organic residues.

(2) Calcination and Characterization

Combined thermogravimetry and differential thermal analyses were performed in air atmosphere to provide information on the temperatures at which organic volatile matter is lost from the dried precipitate upon heating and the key temperature at which the decomposition is completed. Based on these thermal analyses, the dried precipitate was calcinated. The final calcinated product was further characterized by XRD using Cu$K\alpha$ radiation in a Philips PW 3020 diffractometer (Eindhoven, the Netherlands). The specific surface area was determined by nitrogen absorption measurements (BET) using a surface area analyzer (Autosorb-1, Quanta Chroma). The particle size of the calcinated powder was characterized by transmission electron microscopy (TEM) performed on a CM30ST (Philips) microscope operating at 300 kV. An ICP optical emission spectrometer (Spectro Ciros) was used to identify the traces of NO_3^- and NH_4^+ present in the synthesized $SrTiO_3$ nanopowder. X-band electron paramagnetic resonance (EPR) of the nanopowder was recorded at room temperature with a Bruker EMX spectrometer to check possible paramagnetic impurities such as Fe, Mn, etc.

(3) Dilatometry and Sintering

The key feature of nanopowder compaction is the retention of grain sizes within a desirable limit while achieving a density above 90% of the theoretical density. The optimal sintering temperature was decided according to the dilatometry experiments carried out on pre-compacted pellets using a differential dilatometer (BAHR Thermoanalysis DIL 802). The nanocrystalline powders were isostatically pressed at 300 MPa for 5 min. The shrinkage behavior of these green bodies was investigated using dilatometry over the temperature range 30°–1300°C at different heating rates (7.5, 10, and 15 K/min) and holding them isothermally for 15 min under different ambient conditions such as vacuum (1 mbar) and nitrogen. Based on these sintering conditions, the $SrTiO_3$ nanopowder was densified further using single-stage sintering. The grain size of the sintered nanoceramic was determined using a field-emission scanning electron microscope (FESEM) after every stage of each sintering process. It is known that during single-stage sintering, the process is frequently accompanied by a rapid grain growth at high temperatures, especially when the density exceeds 80%. To overcome this problem, a two-stage sintering method,[30] which has been successfully used earlier for nanocrystalline Y_2O_3, is preferred for densification of nanocrystalline $SrTiO_3$. This two-stage sintering technique involves two steps in the heating schedule. Although two-stage sintering resulted in grain sizes less than 100 nm, the densification does not occur uniformly throughout the volume of the pellet (see later). As a result, we preferred uniaxial hot pressing for the densification to avoid significant grain growth and to arrive at a smaller grain size. The density of the sintered pellet was determined using the Archimedes method.

(4) TEM

A common observation while preparing dense ceramics of perovskites such as $BaTiO_3$ and $SrTiO_3$ is the formation of an amorphous phase at the grain boundaries. We have systematically investigated the grain-boundary structure of nanocrystalline $SrTiO_3$ ceramic samples using HRTEM. For TEM investigations of the nanocrystalline $SrTiO_3$ ceramic sample,

standard TEM specimen preparation was carried out starting with a sintered pellet. The preparation steps included cutting of the pellet into a disk, mechanical grinding, and polishing of the disk to a thickness of 100 μm, dimple grinding to a thickness of about 30 μm, and ion-beam milling (Ar^+-ions) to electron transparency of the central region of the disk.

Conventional TEM (JEOL 2000FX, Tokyo, Japan) was used to study the morphology (grain size and shape, defects). The atomic structure in the grain-boundary regions was investigated by HRTEM using a JEOL 4000FX microscope with a point resolution of 0.2 nm and a Philips CM 30ST (point resolution 0.19 nm), respectively. The chemical composition in the grain-boundary region was measured in a scanning TEM (VG HB501UX) using EELS and EDXS.

(5) Electrical Conductivity

The impedance spectroscopic characterization of the electrical behavior in nanocrystalline $SrTiO_3$ (~80 nm) and its comparison with those of sub-micron (~200 nm) and microcrystalline (~2500 nm) $SrTiO_3$ samples is only touched upon briefly as it is a subject of a separate publication.[21] For this purpose, in addition to the 80 nm grain size samples, $SrTiO_3$ ceramics with grain sizes of 200 and 2500 nm were obtained by subsequent heat treatment of the 80 nm sample for about 12 h at 600° and 900°C, respectively, under 250 bar of oxygen pressure and later equilibration at 1 bar of oxygen atmosphere at 1250°C for about 2 h. $YBa_2Cu_3O_{6+\delta}$ was deposited by a pulsed laser to a thickness of ~200 nm to serve as a reversible electrode material. Impedance measurements were performed in the frequency range of 1 Hz–3 MHz (high resolution dielectric analyzer, Novocontrol, Hundsangen, Germany) with 100 mV applied AC voltage in the temperature range of 350°–500°C and in the pO_2 range, 10^{-5}–1 bar.

(6) Complex Dielectric Constant Using Quasi-Optical Submillimeter Spectroscopy

The low-temperature complex dielectric constant of the nanocrystalline $SrTiO_3$ has been obtained from a (non-contact) submillimeter optical spectroscopy measurement that was performed using the coherent source THz spectrometer "Epsilon."[31] The utilized backward wave oscillator source covers the frequency range 180–400 GHz (6–13 cm^{-1}). The measurement was carried out in transmission geometry on a plane-parallel 100 μm thick sample placed in a helium-cooled cryostat. The temperature range was 7–300 K.

III. Results and Discussion

(1) Calcination and Characterization

As described in the experimental procedures, the synthesis and subsequent drying of the gel precipitate in a vacuum oven leads to a light-green-colored dry fluffy powder. Figure 2 presents the combined thermogravimetric and differential thermal analysis of this dried precipitate in air atmosphere. It is found that the weight loss already starts at about 50°C and more significantly at about 560°C as evidenced from a sharp decline in weight,

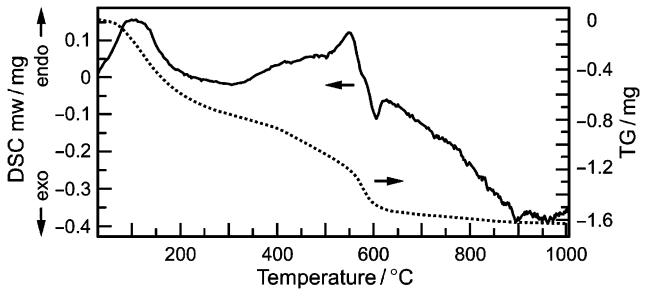

Fig. 2. Thermogravimetry (TG) and differential scanning calorimetry (DSC) of the dried precipitate powder recorded in air at a rate of 7.5 K/min and 7.538 mg of sample in an alumina crucible.

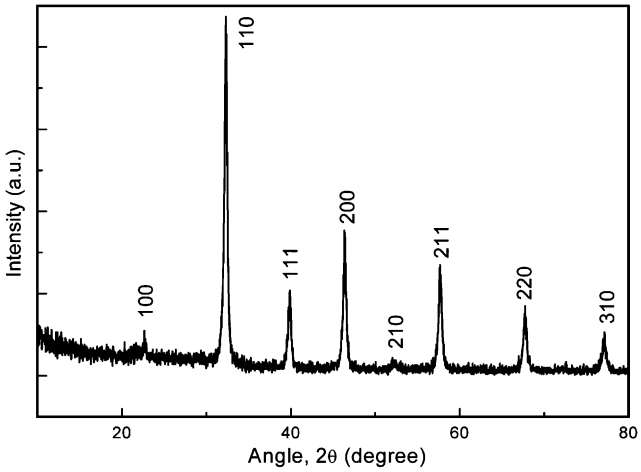

Fig. 3. X-ray diffraction pattern of the $SrTiO_3$ nanopowder obtained by calcination at 1000°C for 1 h. Note that the background observed below 20° is due to the sample holder.

which is accompanied by an exothermic event in differential scanning calorimetry (DSC). Beyond 625°C, only a slight weight change was observed until 1000°C. Although it is sufficient to heat the dried precipitate from 25° until 1000°C for the formation of a well-crystallized nano-sized $SrTiO_3$ phase, our practical experience is that such a slow heating from ambient temperature always resulted in traces of $SrCO_3$ along with the $SrTiO_3$ phase. It is also known that $SrCO_3$ is a common product during the preparation of nanopowders of alkaline titanates such as $BaTiO_3$ and $SrTiO_3$. In order to avoid the trace impurity of $SrCO_3$, the dried precipitate is inserted into a furnace instantly, which had been preset to 450°C and maintained at that temperature for about 2 h. The furnace temperature is then subsequently raised to 1000°C at a rate of 10K/min. This is followed by isothermal calcination for 1 h. This calcination procedure resulted in a white-colored product of $SrTiO_3$ nanopowder free of any carbonate residues as confirmed from the XRD measurements.

Figure 3 presents the XRD pattern of the product obtained upon calcination of the dried precursor at 1000°C for 1 h. Impurity phases such as $SrCO_3$ or TiO_2 were not observed and the X-ray reflections of the calcined product indicated a well-crystallized single phase of $SrTiO_3$.

Figure 4(a) presents the TEM image of the nanopowder calcined at 1000°C for 1 h. As indicated by selected-area electron diffraction (SAED), all observed crystallites can be assigned to the cubic structure of $SrTiO_3$. The average grain size obtained under this calcination condition is about 30 ± 5 nm. The surface area obtained using the BET technique was 47 m^2/g, and the calculated average particle size assuming a spherical shape is 25 nm, which is consistent with the size obtained by TEM. One peculiar feature of the real structure becomes evident from HRTEM micrographs along $\langle 100 \rangle$, which is the formation of perfectly square-shaped defects; see Fig. 4(b). These defects are frequently well aligned with respect to the cubic structure of $SrTiO_3$. Figure 4(c) presents the SAED pattern for the $\langle 100 \rangle$ zone axis referring to the highly crystalline nature of the $SrTiO_3$ nanopowder.

Elemental analysis was performed using the ICP technique. In addition, EPR spectroscopy provided a qualitative estimate of the presence of paramagnetic impurities such as Fe^{3+}, Mn^{2+}, etc. The ICP analysis suggested that the total levels of impurities such as Fe, Al, Na, Ca, Ba, Si, C, etc. are below 250 ppm, with Fe being the major impurity at a level of 125 ppm. ESR analysis has only shown the presence of Fe^{3+} paramagnetic impurity, but no other impurities such as Mn^{2+}, Cu^{2+}, etc. A qualitative analysis of the peak area of the Fe^{3+} signal in the $SrTiO_3$ nanopowder provided an estimate for the amount of this iron impurity to be about 60 ppm. The level of impurity that plays a major

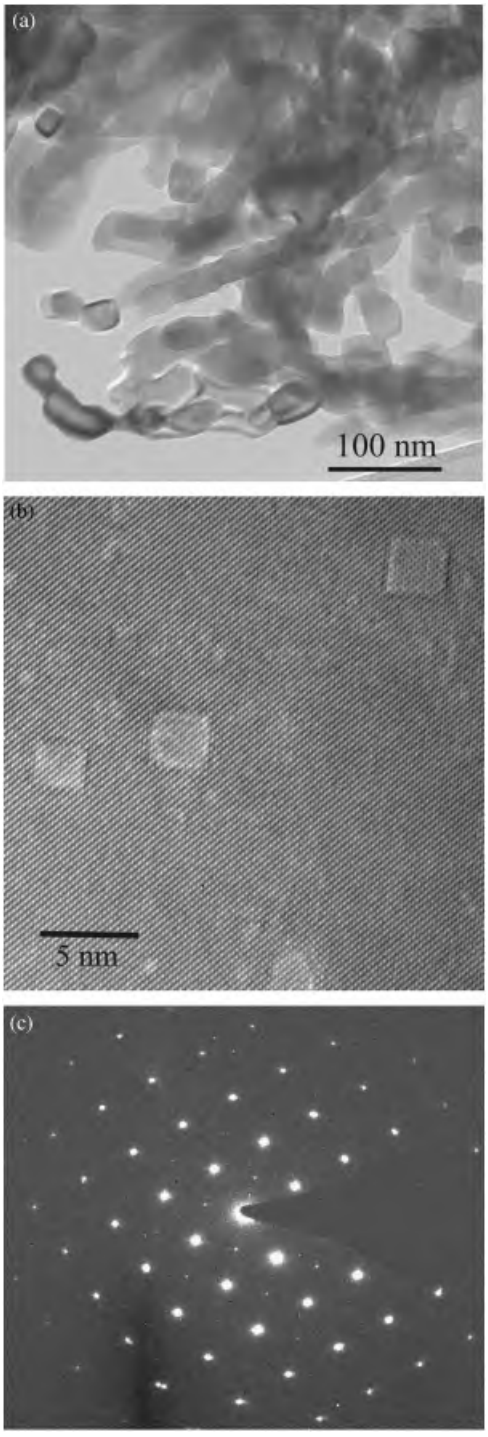

Fig. 4. (a) TEM image of $SrTiO_3$ obtained by calcination of the dried precipitate at 1000°C for 1 h, (b) High-resolution TEM image recorded on $SrTiO_3$ nanocrystalline powder oriented along the ⟨100⟩ zone axis. (c) Selected area electron diffraction pattern along the ⟨100⟩ zone axis.

role for the defect chemistry was also quantified in an indirect way by comparing the bulk conductivity values of the 2500 nm-sized $SrTiO_3$ microcrystalline sample with that of an undoped single crystal $SrTiO_3$. Based on ICP as well as EPR results, it is thus noticed that the bulk impurity, namely Fe^{3+}, contributing to the enhanced conductivity in 2500 nm microcrystalline samples, is about 100 ppm.

Table I summarizes briefly the salient features of the synthesis of $SrTiO_3$ nanopowder using the modified peroxy-based co-precipitation method. It is worth mentioning that this method enables us to achieve a fine powder of $SrTiO_3$.

Table I. Summary of Synthesis of $SrTiO_3$ Nanopowder Using a Modified Peroxide-Based Route and Their Characterization

Starting materials and other required organic materials	$Sr(NO_3)_2$, Ti metal (foil) EDTA, NH_3(aq), HNO_3
Single phase of $SrTiO_3$	Yes (XRD)
Impurity phases such as $SrCO_3$ and TiO_2	No (XRD)
Other impurities	Total impurities <250 ppm (ICP, ESR); Major impurities: Fe, Ba, Ca, Mn, Ta, Si
Impurity level relevant to the defect chemistry	Fe^{3+}, ~100 ppm (ICP, ESR, comparison of conductivity with known bulk behavior of Fe-doped $SrTiO_3$)
Calcination conditions	1000°C for 1 h
Average particle size	30±5 nm (TEM)
Specific surface area	47 m^2/g (BET)
Sr/Ti stoichiometry	1.005 (±0.005)
Densification	93% with grain size <80 nm (see later)

EDTA, ethylene diamine tetraacetic acid; XRD, X-ray diffraction; ICP, inductively coupled plasma; TEM, transmission electron microscopy.

(2) Shrinkage Behavior and Sintering

Figure 5 shows the heating-rate dependence of the shrinkage behavior. It is seen that the sintering at a heating rate of 15 K/min results in a maximum shrinkage of 23.3%, yielding 95% of the theoretical density. However, significant grain growth occurred, resulting in grain sizes in the range 300–500 nm. Figure 6 displays the FESEM image of the fractured surface of this dense pellet. Sintering under similar heating conditions but in an inert atmosphere such as nitrogen showed better performance, achieving an average grain size of 200 nm (Fig. not shown), however, with only about 90% density.

During two-stage sintering of nanocrystalline $SrTiO_3$, the best result was obtained when the pre-compacted pellet was initially heated to 1220°C at a rate of 15K/min under nitrogen atmosphere and subsequently cooled to 1000°C and isothermally held for about 20 h. Figure 7 presents an FESEM image of a fractured pellet obtained through a two-stage sintering process with an average grain size of around 150 nm. Although this procedure was optimized to achieve fine grain size, the densification does not occur uniformly throughout the pellet as seen

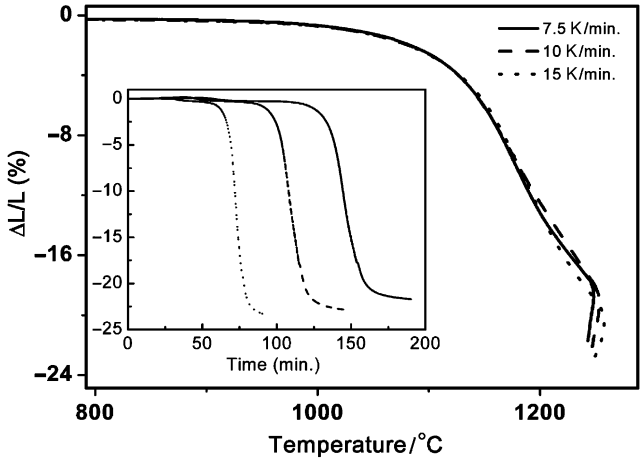

Fig. 5. Dilatometric shrinkage curves of nanocrystalline $SrTiO_3$ as a function of temperature as well as time (inset) under different heating rate conditions (7.5, 10, and 15K/min) in vacuum.

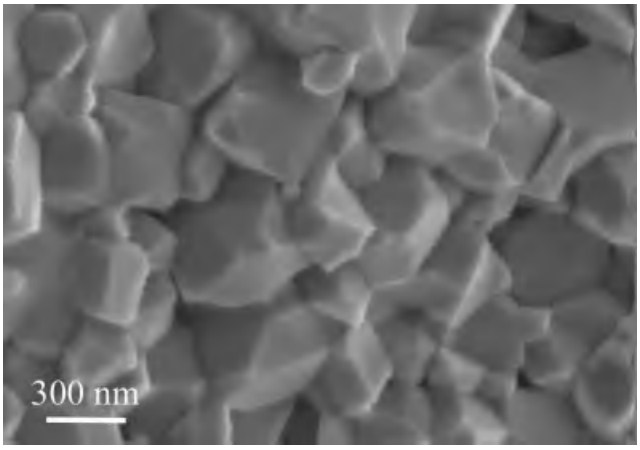

Fig. 6. Field-emission scanning electron microscope image of freshly fractured $SrTiO_3$ ceramic obtained by sintering at 1250°C for 15 min under vacuum.

clearly from Fig. 7. Further compaction has been attempted by a high-pressure two-stage sintering process using a hot press.

The two-stage sintering under high pressure was carried out using a hot press (Dr. Fritsch KG, Germany) in nitrogen atmosphere. The pre-compacted pellet of $SrTiO_3$ nanopowder was heated in a graphite mold to 1060°C at a fast rate of 150K/min in a nitrogen atmosphere and subjected to 125 MPa uniaxial pressure for about 1 min. The temperature was then lowered to 1020°C and retained for 3 min, after which the furnace was switched off. Figure 8 presents the FESEM image of a freshly fractured surface of a pellet obtained using hot pressing. The average grain size calculated from more than 100 grains is close to 80 nm. It may be noted that the whole compaction procedure using the two-stage hot-press sintering technique has been optimized based on several trials. A fast heating rate and high-pressure sintering along with dwell times less than 5 min enabled us to avoid abnormal grain growth and to achieve nearly 93% of the theoretical density. After the hot pressing, extra care was taken to machine the surfaces of this sintered pellet so as to avoid slight contamination by graphite.

(3) TEM Characterization

Figure 9 presents a TEM image of a nanocrystalline $SrTiO_3$ sample, focusing rather on large grains in order to highlight the presence of agglomerated defect structures. Agglomerates of polyhedral-shaped defects were observed mostly within larger grains. It is possible that these "square defects" remain from the

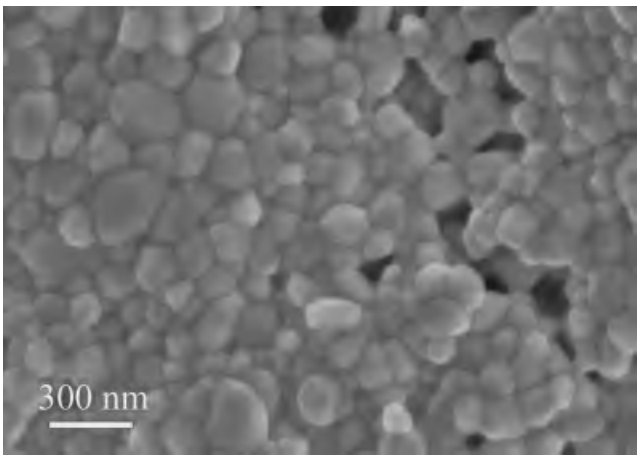

Fig. 7. Field-emission scanning electron microscope image of $SrTiO_3$ nanoceramic prepared using a pressureless two-stage sintering process by heating under nitrogen atmosphere, up to 1220°C at a rate of 15K/min and isothermal sintering at 1000°C for 20 h.

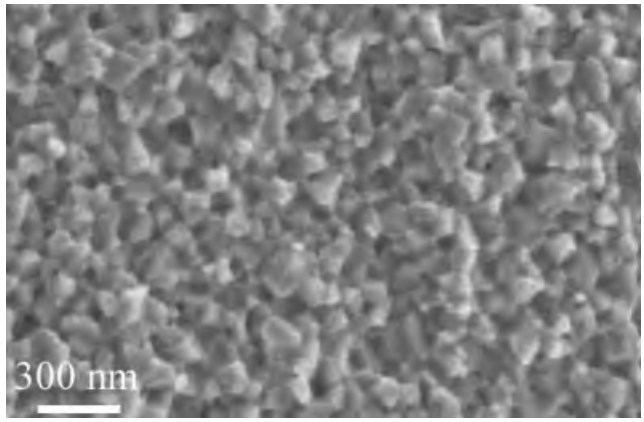

Fig. 8. Field-emission scanning electron microscope image of a freshly fractured surface of a nanocrystalline $SrTiO_3$ pellet obtained using hot pressing, combined with a two-stage sintering process.

nanopowder (see Fig. 4(b)) or due to the porosity while forming agglomerates of hard powder. No change in chemical composition was found in the agglomerate areas based on the EELS analysis. However, thickness measurements performed by EELS showed a smaller apparent thickness at the defect positions, which shows that the defects are voids, presumably formed by agglomeration of vacancies. The depth of such voids corresponds with their lateral size, i.e., the voids are cube-shaped; see also HRTEM micrograph in Fig. 4(b) for the $SrTiO_3$ nanopowder. HRTEM studies revealed that grain boundaries as well as triple-grain junctions are free from intergranular phases. Figure 10 shows a typical HRTEM image of a grain boundary.

From EELS (measurement of the Ti-to-O ratio, not shown) and EDXS (measurement of the Ti-to-Sr ratio, Fig. 11), no variation of the chemical composition across the grain boundaries could be detected within the accuracy of the methods (a typical detection limit for a segregation layer is a tenth of a monolayer).

In summary, within the detection limits, TEM studies show a remarkable chemical homogeneity throughout the nanocrystalline material.

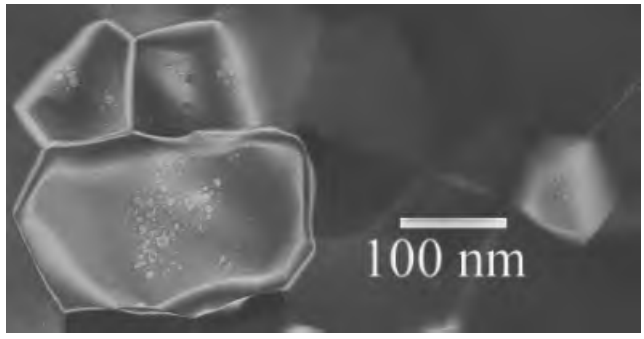

Fig. 9. Transmission electron microscopy overview of the nanocrystalline sample showing cubic-shaped defects.

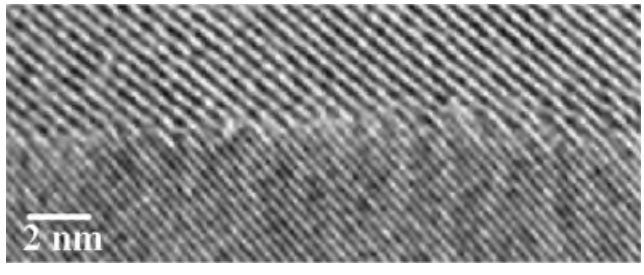

Fig. 10. High-resolution transmission electron microscopy image of a grain boundary in sintered nanocrystalline $SrTiO_3$.

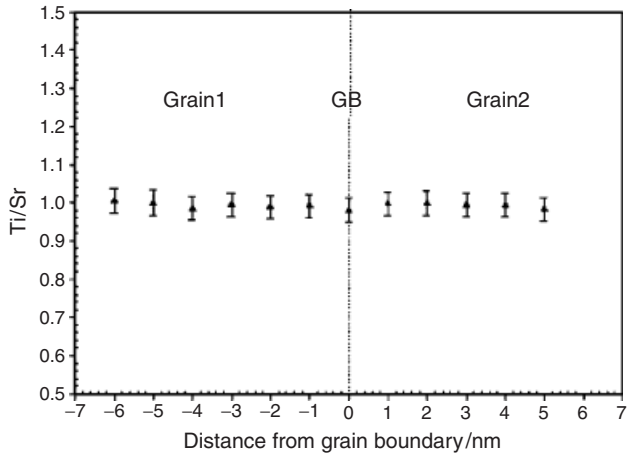

Fig. 11. Cationic concentration ratios ([Ti]/[Sr]) in nanocrystalline $SrTiO_3$, derived from EDXS measurements, starting in a grain, crossing the grain boundary (GB), and continuing in the neighboring grain. Spatial resolution was limited to 2–3 nm by the probe size and beam broadening in the sample.

(4) Impedance Spectroscopy

(A) Electrical Conductivity: Figure 12 presents the impedance plots for the microcrystalline (2500 nm) and nanocrystalline (80 nm) $SrTiO_3$ samples at 420°C. Two semicircles corresponding to both bulk and grain boundaries are clearly identified for the microcrystalline $SrTiO_3$ (2500 nm). In nanocrystalline $SrTiO_3$, on the other hand, only one semicircle referring to the low-frequency signal remains. Thus, unlike microcrystalline $SrTiO_3$, which shows both bulk as well as interfacial contributions to conduction, in nanocrystalline $SrTiO_3$ (80 nm) the bulk contribution to the electrical conduction disappears and space charge effects are observed throughout. In order to know whether the electrical conduction is predominantly due to holes rather than accumulated excess electrons, the pO_2 dependence of the conductivity was performed in the range $1–10^{-5}$ atm., yielding the exponent of +0.21 for the nanoceramic, indicating a hole-dominated conduction process. The space charge length $2\lambda^*$ ($\lambda^* \equiv \lambda\sqrt{4e\Delta\phi/kT}$, where λ is the Debye screening length ($\lambda \equiv \sqrt{\varepsilon\varepsilon_o kT/(2e^2 c_{Fe})}$) and $\Delta\Phi$ is the space charge potential) is deduced to be larger than the grain size, thus confirming the appearance of a mesoscopic phenomenon where the depleted hole regions overlap within the grains. At 420°C, in

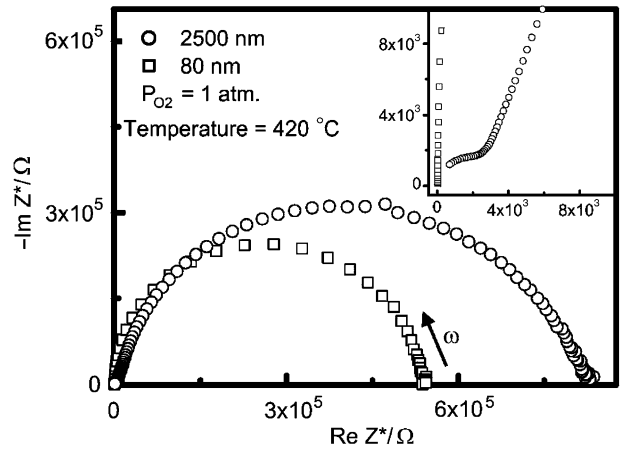

Fig. 12. Impedance plot for microcrystalline (2500 nm) and nanocrystalline (80 nm) samples where the high frequency signal is only present for the microcrystalline sample. The large semicircle is due to grain boundaries. The inset clearly reveals the bulk response at higher resolution for the 2500 nm sample. The geometrical factors (length/area) for the microcrystalline and nanocrystalline $SrTiO_3$ ceramic pellets are 0.118 and 0.547, respectively.

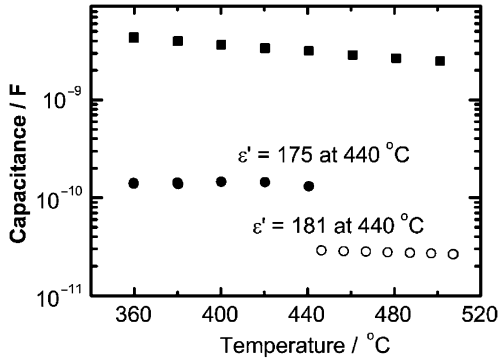

Fig. 13. Variation of capacitance of nanocrystalline and microcrystalline $SrTiO_3$ as a function of temperature. ● and ■ refer to the bulk capacitance and the grain boundary capacitance of the microcrystalline $SrTiO_3$ while ○ refers to the capacitance of nanocrystalline $SrTiO_3$. The values of dielectric constant derived from the capacitance at a selected temperature (440°C) are also included for comparison.

the case of 80 nm grain size, we estimated $\Delta\Phi \approx 0.20$ eV (by taking 100 ppm to be the acceptor density (c_{Fe}) as determined by ICP and ESR analysis) and determined the width of the barrier λ^* to be 48 nm, which is more or less half the grain size. This is consistent with the assumption that the whole grain is depleted and no "bulk" region could be electrically detected (the same calculations for the 200 nm sample, with $\Delta\Phi$ now being higher (0.43 eV) lead to a λ^* value of 71 nm, which is perceptibly less than half the grain size). A detailed discussion of the analysis of the impedance spectra is presented elsewhere.[21]

(B) Capacitance and Dielectric Constant: Figure 13 shows the variation of capacitance for microcrystalline as well as nanocrystalline samples as a function of temperature. It is interesting to note that even though the sample exhibits space charge resistance due to overlap of space charges, it is characterized by a bulk-like capacitance that no longer originates from space charge polarization (space charge does not change with voltage).[19,20] That is, the equivalent circuit of the nanocrystalline $SrTiO_3$ is made up of grain-boundary/space charge resistance in parallel to the bulk capacitance.

It may be noted that the dielectric constant for the nanocrystalline samples and the bulk part of the microcrystalline samples are also included in Fig. 13 for a selected temperature of 440°C. These values are calculated from the total thickness and the area of cross section of the respective samples. It can be noticed that the effective dielectric constant of nanocrystalline $SrTiO_3$ is nearly the same as that of the bulk of microcrystalline sample. Assuming the dielectric constant of the bulk and the grain boundaries of $SrTiO_3$ to be nearly the same,[12,13] the effective thickness of the space charge length ($2\lambda^*$) for the 2500 nm sample is estimated to be 110 nm.

It is often seen in the literature that the capacitance values obtained on single crystals using electrical measurements are quite sensitive to the type of electrodes used.[32] Thus, to overcome such disadvantages, a non-contact measurement such as sub-millimeter optical spectroscopy measurement is highly desirable for the estimation of the dielectric constants of the nanocrystalline $SrTiO_3$ sample. Such a technique has been extensively used on single-crystalline as well as microcrystalline $SrTiO_3$ at a low temperature to look at their permittivity dispersion.[32]

(5) Complex Dielectric Constant Using Quasi-Optical Submillimeter Spectroscopy

The real part of the complex dielectric constant measured down to 7 K in the THz frequency range (180–400 GHz) does not show any dispersion. Therefore, we can consider that the measured frequency range is below the soft-mode frequency and ascribe the full contribution of the $SrTiO_3$ lattice modes to the

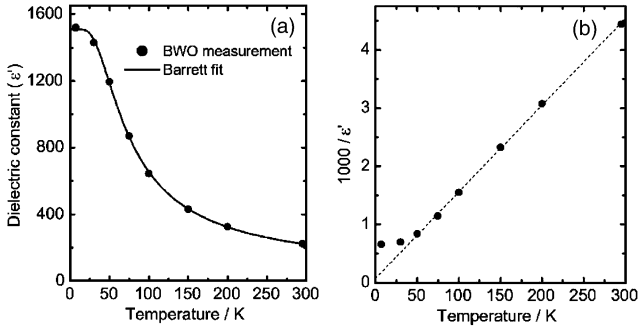

Fig. 14. (a) Dielectric constant of nanocrystalline $SrTiO_3$ sample at 300 GHz as a function of temperature (circles). The line represents a fit using the Barrett expression [Eq. (1)]. (b) Inverse dielectric constant as a function of temperature. The dashed line represents a linear Curie–Weiss law fit of the high-temperature part (above 50 K).

dielectric constant. The temperature dependence of the THz dielectric constant is shown in Fig. 14(a).

At room temperature, the dielectric constant is equal to 225 and it grows upon cooling, reaching $\varepsilon' = 1520$ at 7 K. At temperatures above 50 K, the change of the dielectric constant obeys the Curie–Weiss law as can be seen in Fig. 14(b), which presents the inverse dielectric constant as a function of temperature. Below 50 K, the measured behavior of dielectric constant deviates from the Curie–Weiss law and tends to saturate. Such a behavior is typical for $SrTiO_3$, which belongs to the class of incipient ferroelectrics. The temperature behavior of ε' in this case is better described by the Barrett expression, which models the quantum paraelectric behavior,[33]

$$\varepsilon'(T) = \varepsilon_r + \frac{C}{(\frac{T_1}{2})\coth(\frac{T_1}{2T}) - T_0} \quad (1)$$

where $T_1 = h\nu/k_B$ is a characteristic temperature (ν is the eigenfrequency of a quantum oscillator), T_0 is the generalized Curie–Weiss temperature, C the Curie–Weiss constant, and ε_r the temperature-independent part of the dielectric constant. For $T \gg T_1$, $\varepsilon'(T)$ given by Eq. (1) asymptotically approaches the Curie–Weiss law. The fit of the measured data using Barrett's expression is shown in Fig. 14 (a) and describes the data rather accurately. The fit parameters are $T_1 = 137$ K, $T_0 = 34.4$ K, $C = 5 \times 10^4$, and $\varepsilon_r = 35$. These values are similar to those found for $SrTiO_3$ single crystals.[34] However, the important difference between single crystal and nanocrystalline samples is the value at which the dielectric constant saturates at low temperatures. In our case, $\varepsilon_{max} \approx 1500$ whereas in $SrTiO_3$ single crystal[34] ε_{max} reaches 20 000. This fact indicates that the lattice contribution to the dielectric constant is strongly suppressed in the nanocrystalline $SrTiO_3$. It was also reported for nanocrystalline $SrTiO_3$ with a smaller grain size[35] (less than 44 nm, but only about 50% dense) where the value of the dielectric constant at low temperatures is below 800. A similar effect, however, not so pronounced, has been observed in microcrystalline ceramics[32] where $\varepsilon_{max} \approx 8000$. It was explained by suggesting the dielectric constant of grain-boundary regions to be lower compared with the bulk of the grains. Thus, the average measured dielectric constant of the ceramic sample is suppressed. This suppression can be appreciable in the case of nanocrystalline ceramics where the number of grain-boundary regions having a reduced dielectric constant is rather large. It is well known that diffuse phase transitions can be observed in ferroelectrics with a large defect concentration, including high grain-boundary density. This might also be the reason for the reduced dielectric constants that were attained for nanocrystalline $SrTiO_3$.

IV. Conclusions

A synthesis procedure has been described for the nanocrystalline $SrTiO_3$. The nanopowder is characterized by XRD, TEM, ICP, and ESR measurements. The nanopowder with a well-crystallized cubic phase was found to have a total impurity level less than 250 ppm. Different sintering approaches to obtain a dense ceramic with grain size less than 100 nm have been described. The best sintering result has been achieved by a two-stage sintering process using a hot press yielding 80 nm grain size with a density of 93%. HRTEM analysis of the grain boundaries of the nanoceramic revealed the absence of an amorphous or an intergranular phase. EELS and EDXS characterizations across the grain boundary shows no chemical inhomogeneity within the detectability limits. Square-shaped well-aligned holes are formed both in the nanopowder as well as in the nanoceramic and the reason for this is still not clear. An exciting result based on the impedance spectroscopy measurement is that only a low-frequency semicircle corresponding to the grain boundary and its space charge response appears, and the bulk response disappears due to the overlap of depleted space charge regions. As a result of this mesoscopic situation, although the sample is characterized by the space charge resistance, the capacitance is bulk-like and no longer ascribed to the space charge polarization (space charge does not change with voltage). Evaluation of the low-temperature complex dielectric constant of nanocrystalline $SrTiO_3$ has been performed based on THz optical spectroscopy (non-contact) measurement. Temperature dependence of the dielectric constant suggests an incipient ferroelectric behavior at least down to 7 K, quite similar to what is observed in single crystals. However, the dielectric constant values are strongly suppressed at low temperatures and this is attributed to the influence of a high density of grain boundaries present in nanocrystalline $SrTiO_3$. The dielectric constant values of nanocrystalline $SrTiO_3$ obtained from both the impedance as well as optical measurements are found to be nearly the same.

Acknowledgments

The authors thank J. Jamnik, J. Fleig, R. Merkle, A. J. Bhattacharyya, R. K. Kremer (MPI for Solid State Research), and M. Ruhle (MPI for Metal Research) for useful discussions. The authors also thank G. Cristiani, V. Duppel, U. Klock, P. Senk, G. Gotz (MPI for Solid State Research), S. Kuhnemann, and M. Sycha (MPI for Metal Research) for their technical support.

References

[1]P H. Buffat and J.-P. Borel, "Size Effects on the Melting Temperature of Gold Particles," *Phys. Rev. A*, **13** [6] 2287–98 (1976).
[2]F. Rosei, "Nanostructured Surfaces: Challenges and Frontiers in Nanotechnology," *J. Phys.: Condens. Matter*, **16** [17] S1373–436 (2004).
[3]R. Waser (ed.) *Nanoelectronics and Information Technology*. Wiley-VCH, Weinheim, 2003.
[4]J. Maier, "Ion Conduction in Space Charge Regions," *Prog. Solid State Chem.*, **23** [3] 171–263 (1995).
[5]H. L. Tuller, "Ionic Conduction in Nanocrystalline Materials," *Solid State Ionics*, **131** [1–2] 143–57 (2000).
[6]J. Schoonman, "Nanostructured Materials in Solid State Ionics," *Solid State Ionics*, **135** [1–4] 5–19 (2000).
[7]J. Maier, "Nano-ionics: Trivial and Non-Trivial Size Effects on Ion Conduction in Solids," *Z. Phys. Chem.*, **217** [4] 415–36 (2003).
[8]J. Maier, "Nanoionics: Ion Transport and Electrochemical Storage in Confined Systems," *Nat. Mater.*, **4** [11] 805–15 (2005).
[9]N. Sata, K. Eberl, K. Eberman, and J. Maier, "Mesoscopic Fast Ion Conduction in Nanometer-Scale Planar Heterostructures," *Nature*, **408** [6815] 946–9 (2000).
[10]S. Kim and J. Maier, "On the Conductivity Mechanism of Nanocrystalline Ceria," *J. Electrochem. Soc.*, **149** [10] J73–83 (2002).
[11]P. Balaya, H. Li, L. Kienle, and J. Maier, "Fully Reversible Homogeneous and Heterogeneous Li Storage in RuO_2 with High Capacity," *Adv. Funct. Mater*, **13** [8] 621–5 (2003).
[12]I. Denk, J. Claus, and J. Maier, "Electrochemical Investigations of $SrTiO_3$ Boundaries," *J. Electrochem. Soc.*, **144** [10] 3526–36 (1997).
[13]R. A. De Souza, J. Fleig, J. Maier, O. Kienzle, Z. Zhang, W. Sigle, and M. Ruhle, "Electrical and Structural Characterization of a Low-Angle Tilt Grain Boundary in Iron-Doped Strontium Titanate," *J. Am. Ceram. Soc.*, **86** [6] 922–8 (2003).

[14]P. C. McIntyre, "Equilibrium Point Defect and Electronic Carrier Distributions Near Interfaces in Acceptor-Doped Strontium Titanate," *J. Am. Ceram. Soc.*, **83** [5] 1129–36 (2000).
[15]V. Ravikumar, R. P. Rodrigues, and V. P. Dravid, "An Investigation of Acceptor-Doped Grain Boundaries in $SrTiO_3$," *J. Phys. D: Appl. Phys.*, **29** [7] 1799–806 (1996).
[16]R. Hagenbeck and R. Waser, "Influence of Temperature and Interface Charge on the Grain-Boundary Conductivity in Acceptor-Doped $SrTiO_3$ Ceramics," *J. Appl. Phys.*, **83** [4] 2083–92 (1998).
[17]Z. L. Zhang, W. Sigle, F. Phillipp, and M. Ruhle, "Direct Atom-Resolved Imaging of Oxides and Their Grain Boundaries," *Science*, **302** [5646] 846–9 (2003).
[18]R. Moos and K.-H. Hardtl, "Defect Chemistry of Donor-Doped and Undoped Strontium Titanate Ceramics between 1000 and 1400°C," *J. Am. Ceram. Soc.*, **80** [10] 2549–62 (1997).
[19]M. Leonhardt, J. Jamnik, and J. Maier, "In Situ Monitoring and Quantitative Analysis of Oxygen Diffusion Through Schottky Barriers in $SrTiO_3$ Bicrystals," *Electrochem. Solid-State Lett.*, **2** [7] 333–5 (1999).
[20]X. Guo, J. Fleig, and J. Maier, "Separation of Electronic and Ionic Contributions to the Grain-Boundary Conductivity in Acceptor-Doped $SrTiO_3$," *J. Electrochem. Soc.*, **148** [9] J50–3 (2001).
[21]P. Balaya, J. Jamnik, J. Fleig, and J. Maier, "Mesoscopic Electrical Conduction in Nanocrystalline $SrTiO_3$," *Appl. Phys. Lett.*, **88** [6] 062109 (2006).
[22]M. Kakihana, T. Okuba, M. Arima, Y. Nakamura, M. Yashima, and M. Yoshimura, "Polymerized Complex Route to the Synthesis of Pure $SrTiO_3$ at Reduced Temperature: Implication for Formation of Sr–Ti Heterometallic Citric Acid Complex," *J. Sol–Gel Sci. Technol.*, **12** [2] 95–109 (1998).
[23]V. Kumar, "Solution–Precipitation of Fine Powders of Barium Titanate and Strontium Titanate," *J. Am. Ceram. Soc.*, **82** [10] 2580–4 (1999).
[24]J. Poth, R. Haberkorn, and H. P. Beck, "Combustion-Synthesis of $SrTiO_3$ Part I. Synthesis and Properties of the Ignition Products," *J. Eur. Ceram. Soc.*, **20** [6] 707–13 (2000).
[25]W. F. Zhang, Z. Yin, M. S. Zhang, D. L. Du, and W. C. Chen, "Roles of Defects and Grain Sizes in Photoluminescence of Nanocrystalline $SrTiO_3$," *J. Phys.: Condens. Matter*, **11** [29] 5655–60 (1999).
[26]J. J. Urban, W. S. Yun, Q. Gu, and H. Park, "Synthesis of Single-Crystalline Barium Titanate and Strontium Titanate," *J. Am. Chem. Soc.*, **124** [7] 1186–7 (2002).
[27]D. Chen, X. Jiao, and M. Zhang, "Hydrothermal Synthesis of Strontium Titanate Powders with Nanometer Size Derived from Different Precursors," *J. Euro. Ceram. Soc.*, **20**, 1261–5 (2000).
[28]H. Herrig and R. Hempelmann, "Microemulsion Mediated Synthesis of Ternary and Quaterbary Nanoscale Mixed Oxide Ceramic Powders," *Nanostruc. Mater.*, **9** [1–8] 241–4 (1997).
[29]E. R. Camargo and M. Kakihana, "Peroxide-Based Route Free from Halide for the Synthesis of Lead Titanate Powder," *Chem. Mater.*, **13** [4] 1181–4 (2001).
[30]I. W. Chen and X. H. Wang, "Sintering Dense Nanocrystalline Ceramics Without Final-Stage Grain Growth," *Nature*, **404** [6774] 168–71 (2000).
[31]G. Kozlov and A. Volkov, "Coherent Source Submillimeter Wave Spectroscopy"; pp. 51–109 in *Mellimeter and Submillimeter Wave Spectroscopy of Solids*, Edited by G. Gruner. Springer, Berlin, 1998.
[32]J. Petzelt, T. Ostapchuk, I. Gregora, I. Rychetsky, S. Hoffmann-Eifert, A. V. Pronin, Y. Yuzyuk, B. P. Gorshunov, S. Kamba, V. Bovtun, J. Pokorny, M. Savinov, V. Porokhonskyy, D. Rafaja, P. Vanek, A. Almeida, M. R. Chaves, A. A. Volkov, M. Dressel, and R. Waser, "Dielectric, Infrared, and Raman Response of Undoped $SrTiO_3$ Ceramics: Evidence of Polar Grain Boundaries," *Phys. Rev. B.*, **64**, 184111 (2001).
[33]J. H. Barrett, "Dielectric Constant in Perovskite Type Crystals," *Phys. Rev.*, **86** [1] 118–20 (1952).
[34]K. A. Muller and H. Burkard, "$SrTiO_3$: An Intrinsic Quantum Paraelectric Below 4 K," *Phys. Rev. B*, **19** [7] 3593–602 (1979).
[35]T. K. Song, J. Kim, and S.-I. Kwun, "Size Effects on the Quantum Paraelectric $SrTiO_3$ Nanocrystals," *Solid State Commun.*, **97** [2] 143–7 (1996). □